Chemistry–A European Journal
Research Article
doi.org/10.1002/chem.202403058
Chemistry Europe
European Chemical Societies Publishing
www.chemeurj.org

Odorant Binding Proteins Facilitate the Gas-Phase Uptake of Odorants Through the Nasal Mucus

Massimiliano Paesani,[a, b] Arthur G. Goetzee,[a] Sanne Abeln,[a, c] and Halima Mouhib*[a]

Mammalian odorant binding proteins (OBPs) have long been suggested to transport hydrophobic odorant molecules through the aqueous environment of the nasal mucus. While the function of OBPs as odorant transporters is supported by their hydrophobic beta-barrel structure, no rationale has been provided on why and how these proteins facilitate the uptake of odorants from the gas phase. Here, a multi-scale computational approach validated through available high-resolution spectroscopy experiments reveals that the conformational space explored by carvone inside the binding cavity of porcine OBP (pOBP) is much closer to the gas than the aqueous phase, and that pOBP effectively manages to transport odorants by lowering the free energy barrier of odorant uptake. Understanding such perireceptor events is crucial to fully unravel the molecular processes underlying the olfactory sense and move towards the development of protein-based biomimetic sensor units that can serve as artificial noses.

Introduction

To trigger a signal in olfactory perception, odorant molecules and volatile compounds are bound to first travel by air through the nasal cavity, and subsequently cross the air-mucus interface to selectively bind their target odorant receptors (ORs) embedded in the membrane of the olfactory epithelium. During this process, odorant binding proteins (OBPs) are thought to facilitate the transport of hydrophobic odorants through the hydrophilic nasal mucus, and thus manifest the very first level of molecular mechanisms underlying the olfactory sense.[1–3] Although this provides us with a general understanding of odorant binding, the exact underlying mechanisms of action have not yet been reported at an atomistic scale. In particular, no attention has been paid to the intrinsic properties and the structural dynamics of the odorant molecules during the process. Little is known about relevant conformations that are sampled by the odorant molecule within the protein binding site. Here, we hypothesize that OBPs facilitate the transport of odorants through the air-mucus interface by mimicking the gas-phase environment through their characteristic hydrophobic binding pocket. To test our hypothesis and shed more light into the function of OBPs as odorant transporters, we focus on characterizing the conformational landscape explored by odorant molecules within three different states: the gas phase, the aqueous phase, and the protein environment. The aqueous phase hereby represents the hydrophilic nasal mucus (simplified view). Using porcine OBP (pOBP) and its identified binding partner carvone (see Figure 1),[4] our approach targets studying the initial step in the olfactory process: the uptake of hydrophobic odorants from the gas-phase to the solvated phase. Hereby, we focus on how the conformational space sampled by the odorant is affected in these three environments. Characterising the conformations that are explored by the odorant molecule during this process allows to understand if and how OBPs facilitate their transport through the hydrophilic mucus.

To obtain atomistic detail into this process, a multi-scale computational approach is required to take all the different

[a] M. Paesani, A. G. Goetzee, Dr. S. Abeln, Dr. H. Mouhib
Department of Computer Science, Bioinformatics, Vrije Universiteit Amsterdam, De Boelelaan 1105, 1081 HV Amsterdam,
The Netherlands
E-mail: h.mouhib@vu.nl
[b] M. Paesani
Van't Hoff Institute for Molecular Sciences, Universiteit van Amsterdam, Science Park 904, 1090 GD Amsterdam, The Netherlands
[c] Dr. S. Abeln
Department of Information and Computing Sciences, Department of Biology, Utrecht University, Heidelberglaan 8, 3584 CS, Utrecht, The Netherlands

Supporting information for this article is available on the WWW under https://doi.org/10.1002/chem.202403058

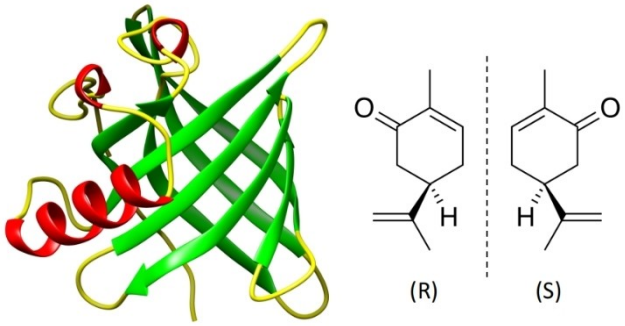

Figure 1. Left: Structure of porcine odorant binding protein (pOBP, PDB-ID: 1A3Y[5]). The eight anti-parallel beta-sheets of pOBP are typical for members of the lipocalin family and form a strongly hydrophobic binding environment for small organic molecules. Secondary elements; beta-sheets, alpha helices, and loops are colored in green, red, and yellow, respectively.[6] Right: The two enantiomeric forms of carvone (*(R)*- and *(S)*-enantiomer).

states into proper consideration. A simplified overview of our muti-scale approach is provided in Figure 2. Here, stands the isolated odorant in the gas-phase as the initial step in the olfactory process, before subsequently moving into the solvated phase and the protein environment. While the first state is best described at quantum chemical level, the latter two correspond to an increase in size of the molecular system of interest and requires the use of classical molecular dynamics (MD) and enhanced sampling techniques.[7] To carry out the full conformational analysis of organic molecules such as carvone in the gas-phase, quantum chemical calculations may provide high-quality geometries that can be directly validated using high-resolution microwave spectroscopy experiments.[8] Rotational spectroscopy methods have previously been used successfully for conformational studies in fragrance research,[9] and are widely applied for the characterization of biomolecules[10–12] and complex systems[13–15] in the gas-phase. The unique experimental setup provides the advantage of studying the intrinsic properties of molecular targets in their isolated states, i.e., in the gas-phase, by identifying different conformations.[16,17] This isolated state is the most simple state to study before looking at solvation effects,[18,19] and the effects of the protein environment.[20] In this work, we directly validate the quantum chemical models of carvone with experimental data from high-resolution microwave spectroscopy experiments available in the literature.[21,22] The validated quantum chemical structures are then used to guide and set-up the MD simulations to quantify and characterize the conformational landscape of the odorant in the gas phase, in water, and within the pOBP binding pocket. We perform MD simulations of carvone *in vacuo*, in explicit water, and in complex with pOBP.[5] To guarantee their physical relevance, our protein simulations are guided using available experiments on the bound state of carvone and pOBP.[2,4] To further quantify the bound state of the protein-odorant complex, the free energy landscape of the carvone uptake through pOBP needs to be considered. Here, to quantify the stability and the free energy difference between the bound and unbound states, volume-based (VB) metadynamics provides a powerful enhanced sampling technique.[23] The setup and computational details of the production runs for all computational models at the different scales are provided in the electronic supporting information (SI).

Results and Discussion

Carvone Adopts Two Sets of Distinct Conformations in the Gas-phase

Prior to looking at the structure and dynamics of carvone inside the protein complex, the conformational landscape of the molecule needs to be characterized without any influence from the environment. This step describes carvone in its isolated state in the gas phase using high level quantum chemical methods. To this aim, several starting conformations of carvone were generated for the optimizations at quantum chemical level through rotation around the sp^3 hybridized C–C bonds, including chair and boat conformations of the carbon cycle. The

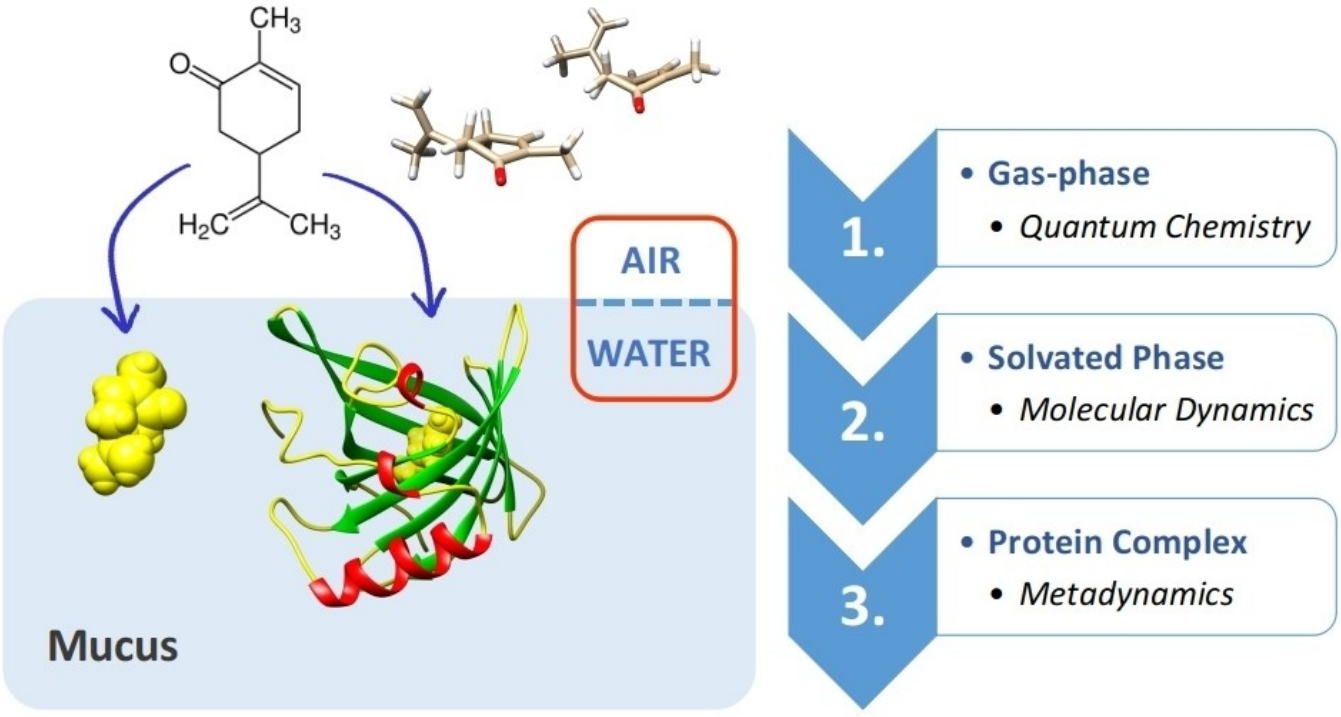

Figure 2. Overview of the multi-scale approach implemented in this work to study the transfer of carvone from the gas- to the aqueous phase, and in its bound state with pOBP. This approach allows to compare the conformational space that is explored by carvone in the different environments using adapted computational techniques. The computational set up for each scale is provided in the SI.

input structures were subsequently optimized using the hybrid exchange-correlation functional of Becke-Lee-Parr (B3LYP)[24,25] from density functional theory, and the post-Hartree Fock method Moller-Plesset perturbation theory of second order (MP2) method[26] in combination with the 6-311++G(g,p) Pople triple-zeta basis set. The quantum chemical computations yielded six stable conformers with relative energy differences below 10 kJ/mol for each carvone enantiomer, which were verified using harmonic frequency calculations to exclude transition states (see SI for full details). From a structural point of view, the six different conformers can be clustered into two distinct subsets based on the orientation of the isopropenyl group: one subset with an equatorial orientation (hereafter referred to as subset I) and another subset with an axial orientation of the isopropenyl moiety (hereafter referred to as subset II). The structural superposition of the *(R)*-carvone conformers into subset I and subset II is shown in Figure 3. Note that the six conformers of carvone have been labeled as conformer 1, 2, 3, 4, 5, and 6, according to their increasing relative energies from the global minimum (conformer 1) as obtained at the MP2/6-311++G(d,p) level of theory. Subset I and II each comprise 3 of the six conformers optimized at quantum chemical level (subset I: conformers 1, 3, and 5; and subset II: conformers 2, 4, and 6, see Figure S2). Note that within each subset, the three conformations differ by the rotation of the sp^3 hybridized rotatable bond between the carbon-cycle and the isopropenyl group (see Figure 3). Using high-resolution microwave spectroscopy experiments, two stable conformers were identified in the gas-phase spectra by Moreno *et al.*[21] under molecular beam conditions. Both experimentally observed conformers exhibit an equatorial orientation of the isopropenyl group and correspond to structures found in subset I (see Figure 3). The equatorial orientation of side groups and substituent is often energetically favored over axial orientations, unless strong intramolecular interactions favor the latter. The reported experimental rotational constants are in good agreement with the geometries optimized at the MP2 level of theory (below 1% deviation) and the most abundant energy conformer observed in the experiment corresponds to the global minimum identified at quantum chemical level using both, the MP2 and the B3LYP method. It should also be noted that enantiomers possess the same rotational constants and therefore cannot be distinguished in the reported rotational spectroscopy experiment.[21] However, for the sake of completeness and also to validate the computational biology models, we included both, *(R)*- and *(S)*-carvone throughout all computational methods in our study. The optimized structures of the lowest energy conformer at the MP2 level of theory serve as starting point for the molecular dynamics simulations of both enantiomers of carvone in explicit water, to mimic the hydrophilic nasal mucus, *in vacuo*, and in the protein binding cavity. The full overview of the quantum chemical results including the Cartesian coordinates, relative energies and charges of all optimized conformers for both carvone enantiomers is provided in Section 1 of the SI.

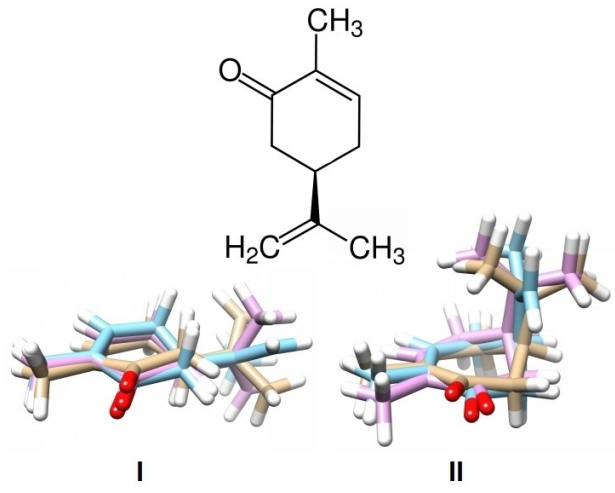

Figure 3. Structural superposition of the optimized conformers of *(R)*-carvone at the MP2/6-311++G(d,p) level of theory using the UCSF Chimera program package. Note that the six energy minima can be classified into two distinct subsets of conformations with an (I) equatorial, and (II) axial orientation of the isopropenyl moiety. All optimizations were carried out using the GAUSSIAN16 program package[27] The conformers clustered within subset I and subset II correspond to the conformers 1, 3, 5 and to the conformers 2, 4, 6, respectively (see Figure S2 for details). The full overview of the quantum chemical results is provided in section 1 of the SI.

pOBP Remains Unchanged upon Binding

Before looking into the bound form of the carvone and pOBP protein-ligand complex (holo form), the structure and dynamics of pOBP in its free and unbound state (apo form) need to be considered. Like most mammalian OBPs (with the exception of bovine OBP)[28], pOBP forms a stable monomer in solution. Subsequently, the holo form including one carvone enantiomer at a time can be tackled. Overall, the beta-barrel structure of pOBP is extremely stable, and experiments have shown that even truncated mutants missing the first eight residues of at the N-terminal maintain their stability in solution.[29,30] To analyze the stability and monitor the flexibility of the monomeric protein, we performed molecular dynamics simulations using the AMBERff99SB-ILDN force field implemented in GROMACS (version 2020.3). Altogether, 10 explicit water simulations of 50 ns were run for each set-up: pOBP in its apo-form and two holo-forms, i.e., in complex with either the *(R)*- or the *(S)*-carvone enantiomer. A detailed description of the simulation set-up is given in Section 2 of the SI. From the MD production runs, the root mean square deviation (RMSD) allows us to monitor the overall changes of the pOBP structure and showed that there is no difference between the holo-form and the apo-forms of pOBP. In addition to the RMSD, we also define tree cross-barrel distances between opposing residues around the center of mass of the protein as specific order parameters to observe any changes of the binding site (see SI Figure S5). Again, there is no difference between the apo- and holo-forms of pOBP (see Figure S4 and S6). This means that the overall structure of the binding cavity is not impacted by the presence of the ligand throughout the simulations. These findings are in agreement with observations from experiments, where it was

shown through several studies that mammalian OBPs are not likely to undergo any conformational changes upon ligand binding.[29,30] Putting this is perspective of the putative transporter function of OBPs, we note that the binding cavity of pOBP has a volume of approximately 500 Å^3,[31] while a carvone enantiomer will take around 200 Å^3 of space (estimating 18 Å^3 for each non-hydrogen atom). There is thus sufficient room for carvone to adapt different poses and conformations inside the binding pocket without impacting the overall protein structure. This is further supported by X-ray data of several pOBP-odorant complexes, and aligns with the view of the putative transporter function of OBPs in the nasal mucus,[5,31] providing the opportunity to study the conformational space explored by carvone within the protein binding pocket.

Conformational Sampling of Carvone Shows that pOBP Provides an Ideal Hydrophobic Environment to Mimic the Gas Phase

In addition to the simulations of the pOBP-carvone complex, both enantiomers of carvone were simulated using molecular dynamics in explicit water and under *in vacuo* conditions to compare their structure and dynamics in all three states: gas (*in vacuo*), mucus (explicit water), and protein environment (pOBP-carvone complex). Since the predicted energy differences between the six different conformations of carvone are estimated to lie below 10 kJ/mol at quantum chemical level, both conformational subsets shown in Figure 3 are likely to be observed in the gas-phase simulations. Within a different environment such as water or inside the protein, however, the conformational space is likely to be confined to a smaller subspace due to the influence of the environment. For instance, the hydrophobic interface of carvone is likely to be minimized as a results of the hydrophobic effect. It is known that the curvature of small solutes affects the hydrophobic effect of the molecules and therefore, one conformational subset of carvone could be favored over the other depending on the environment.[32,33] To monitor the conformational landscape of carvone during the simulations, we define a molecular distance *d* between two carbon atoms (one in the isopropenyl group and one in the hydrocarbon ring, see Figure 4) as an intrinsic order parameter. This allows us to distinguish the conformational state of carvone, i.e., whether it is sampling the states in subset I or sampling the states in subset II. Figure 4 depicts the order parameter *d* during the interconversion of conformer 1 (representing the structures of subset I) to conformer 6 (representing the structures of subset II) through the connecting transition state optimized at the MP2/6-311++G(d,p) level of theory. This order parameter *d* is ideal to explicitly distinguish between the two different subsets of carvone. It is certainly more insightful than the RMSD for such a small molecular system, since the RMSD may be ambiguous to distinguish between the different conformations. Next to the distance *d*, the radius of gyration R_G may also serve as a useful measure since the curvature of carvone is clearly different between the two subsets (see Figure 3 Section 2 of the SI).

Throughout 10 MD simulations of 50 ns using randomized starting velocities for each production run, both enantiomers of carvone are sampled in the gas and inside the protein environment, allowing us to estimate the free energy barrier between the two states. In explicit water however, the barrier of interconversion between the structures in subset I and subset II of carvone is too high and the timescale of the simulations does not allow proper sampling between the different states. Therefore, enhanced sampling techniques are needed to accelerate the simulations and determine the barrier height in explicit water. Here, we apply umbrella sampling (US) which is a powerful technique to estimate the relative free energy of different states along a defined reaction coordinate. Using

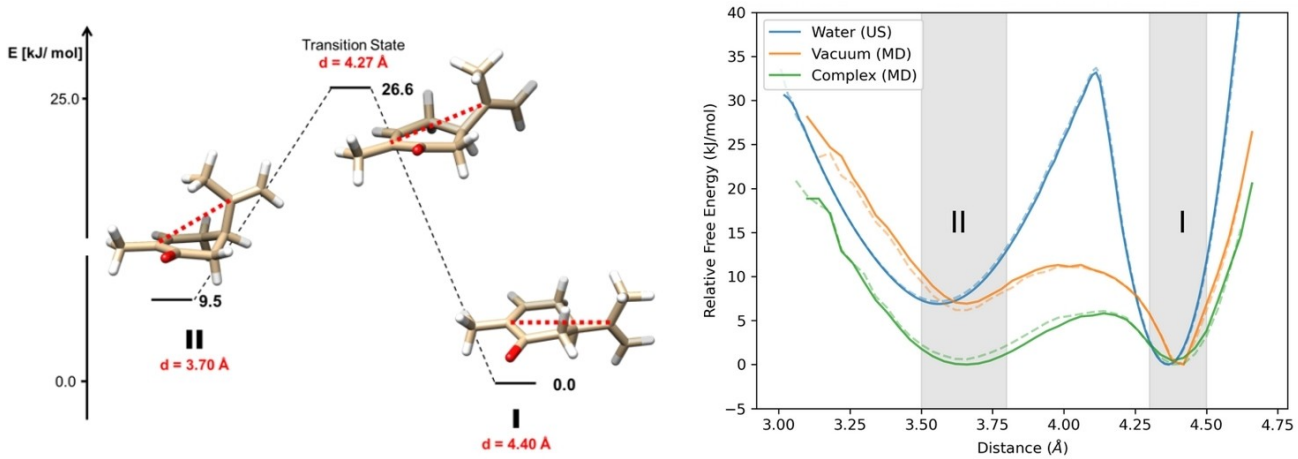

Figure 4. Left: Reaction coordinate for the interconversion of *(R)*-carvone from conformer 1 (global minimum and representative conformer for subset I, see Figure 3) through the joint transition state to conformer 6 (representative conformer for subset II, see Figure 3). The distance between the two carbon atoms used as order parameter *d* to distinguish the different conformational states of carvone in the gas phase is highlighted in red. The structures and relative energies in kJ/mol were obtained after optimization at the MP2/6-311++g(d,p) level of theory; Right: Free energy surfaces of *(R)*-carvone in 3 different phases: water (Water), gas (Vacuum), and protein environment (Complex), the free energy surfaces of *(S)*-carvone are depicted as dotted lines. US and MD: umbrella sampling simulations and molecular dynamics simulations, respectively. See SI for further details.

conformer 1 (representing the structures in subset I) and conformer 6 (representing the structures in subset II) as the start and end point of the US simulation, respectively, and the distance *d* as reaction coordinate to link the two states, we were able to estimate the barrier to interconversion between the two carvone subsets I and II. The corresponding free energy plots in all three states, *in vaccuo*, in explicit water, and inside the protein environment, are shown in Figure 4. In the gas phase, both conformational ensembles are sampled, although a preference can be observed towards the conformations of subset I, with an equatorial orientation of the isopropenyl group. This is in agreement with the quantum chemical calculations, which show that these conformations are energetically more favorable than subset II, which contains conformers of axial orientation. Although the energetically favored state remains unchanged in the explicit water simulations, the barrier height is significantly higher than in the gas phase and inside the protein binding cavity. In the gas phase and inside the binding cavity of pOBP the barrier height is significantly lower, which allows carvone to fully explore its conformational landscape. This indicates that the protein environment is able to mimic the gas phase, and we hypothesize that this *gas-like environment* is what allows hydrophobic odorants to cross the interface between the gas and the hydrophilic mucus. To gain more insights into the nature of the binding and the conformational changes undergone by carvone during the transportation through the mucus, the distribution of water molecules around carvone within the different solvated environments, i.e., in explicit water and inside the protein binding pocket, should be taken into account. The density of water around carvone within a 5 Å radius as well as the radial distribution function plots for the different production runs are provided in the SI (see Figure S10). The analyses show that the protein binding pocket contains almost no water molecules throughout the simulations. The distribution of the water molecules closest to carvone in the different simulations is shown in Figure 5. In explicit water, carvone is fully surrounded by solvent molecules and cannot freely sample its conformational space, while within the protein environment there are no water molecules within a radius of 7 Å around the carvone molecule and both conformational subsets are sampled.

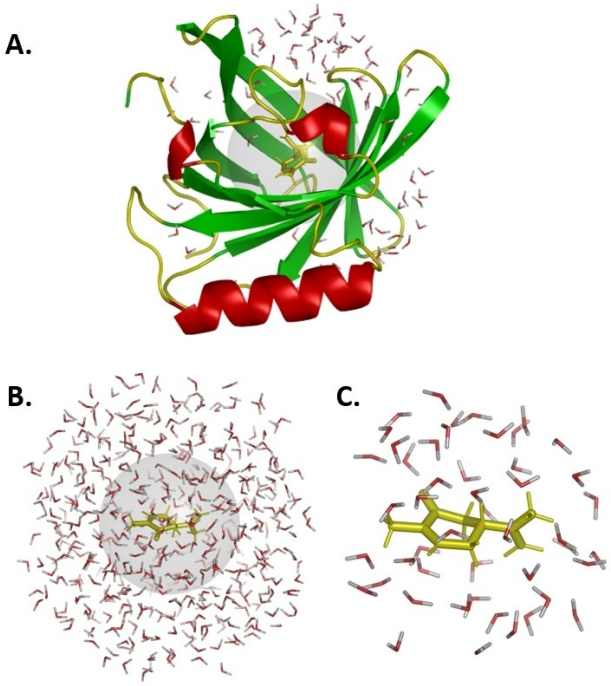

Figure 5. Snapshots from simulation runs of *(R)*-carvone in the two solvated environments. **A**: Inside the protein binding pocket. **B**: In explicit water. The center of the light-grey spheres is superimposed on the center of mass of carvone. The radii of the spheres are fixed to 7 Å and the water molecules within a distance of 15 Å are shown. **C**: Zoom on the light-grey sphere shown in **B**.

Characterizing the Lowest Energy State: Insight into the Free Energy Landscape of the Carvone-pOBP Complex

From these findings we hypothesize that the bound protein-odorant complex is energetically favored and that this can be directly linked to the transporter function of pOBP. To simulate the bound and unbound form of the carvone and pOBP complex and estimate the change in free energy between the bound and the unbound state, the application of enhanced sampling techniques is required.[34] Enhanced sampling techniques such as metadynamics, steered molecular dynamics, or umbrella sampling allow to characterize binding affinities within the protein complex. These methods usually rely on the intrinsic molecular properties of the problem at hand, such as the unbinding pathway, to properly define the reaction coordinate around which the free energy landscape should be sampled. However, although putative binding pathways and affinities have been reported for several OBPs including pOBP (see Table 1),[1,3,35] these findings cannot be directly applied to the carvone-pOBP complex, as they, e.g., focus primarily on studying the binding affinity from selected mutants of pOBPs for chiral discrimination.[2,4] Since no clear unbinding pathway has been reported for carvone and pOBP in the literature, we cannot define reliable collective variables (CVs) for our system. In such as case, VB metadynamics, a recent extended version of funnel-based well-tempered metadynamics),[36] is the method of choice to estimate the free energy of binding of our system, as it does not require prior knowledge of the unbinding pathway.[6,23,37] Unlike funnel metadynamics,[38] which samples the free energy along a predefined reaction coordinate, VB-MD samples all possibilities of the ligand to escape from the protein binding site within a defined sphere until it reaches the unbound state.[23] This method is adapted to take numerous unbinding pathways of a protein-ligand complex into account and estimate relative free-energy differences that are relatively well comparable to experimental values. Figure 4 shows the resulting free energy landscapes for the unbinding of *(R)*- and *(S)*-carvone projected on two intuitive CVs: the distance of carvone from the center of mass of the protein (ρ in nm), and the coordination number (CN), which captures the amount of non-covalent contacts between the respective carvone enantiomer and the residues of the pOBP binding site. These two

Table 1. Odor descriptors, solubilities, and binding affinities of selected odorants previously reported to bind wildtype pOBP.[2,31]

Odorant	Odor Descriptors[a]	Solubility [mg/L][a]	Binding affinity [mu M][b]	Ref.[c]
Benzophenone	sweet, rosy, herbal	137	3.6 ± 0.6	[31]
Benzylbenzoate	balsamic, herbal	15.39	3.9 ± 0.8	[31]
Dihydromyrcenol	citrus, bergamot	252.2	0.8 ± 0.1	[31]
Undecanal	floral, waxy, citrus	14.27	0.7 ± 0.2	[31]
(R)-Carvone	spearmint, herbal	1310	0.39/0.42[d]	[2]
(S)-Carvone	caraway, minty	1300	0.39/0.42[d]	[2]
(R)-Menthol	minty-fresh	456	1.2/1.8[d]	[2]
(S)-Menthol	minty-fresh	456	1.2/1.8[d]	[2]
Thymol	thyme-like, medicinal	900	2.5 ± 0.4	[31]

[a] Odor descriptions and solubilities (in water at 25 °C) are given as provided on http://www.thegoodscentscompany.com/ (04.08.2024). [b] IC50 values. For *(R)*/*(S)*-carvone and Menthol the $1/K_D$ values are provided.[2] [c] references for the binding affinities. [d] Values estimated from data in ref [2].

CVs allow to get an accessible description of the molecular structure underlying the protein-odorant complex. A detailed description of VB metadynamics, the definition of the CVs, and details of the simulation set up including the free energy landscapes for different radii of the sphere (<28 Å), are provided in the SI. The relative free energy of the bound and unbound states can be obtained by subtracting the energy values of the global minima (the bound state) by the energy of the unbound states (cf. Table 2). Hereby, the unbound state can be defined somewhat arbitrarily as described by Capelli *et al.*.[23] We thus define the unbound state in the range of $\rho > 2$ Å and a low CN (CN <10). The bound state on the other hand can be found in the region close to the center of mass $250 <$ CN < 350 and $\rho > 0.5$ Å. The structure of the two states and their relative locations on the free energy landscape are depicted in Figure 6. In agreement with experimental findings, we observe very similar contours for the free energy landscape of *(R)*- and *(S)*-carvone, indicating indeed that the wild-type pOBP does not distinguish between the two enantiomeric forms.[2,4] Although the barrier between the bound and the unbound state is relatively high (around 70 kJ/mol), it should be noted that at the biological level, OBPs are most likely concentrated and operational at the air-mucus interface. In human olfaction, their presence has been reported in the mucus covering the olfactory cleft, where the sensory olfactory epithelium is located which again strongly suggest their role as odorant carriers. This is in alignment with our hypothesis that odorant binding proteins serve as transporters helping odorants to cross the air-mucus interface. As such, they should be non-selective to be able to transport a maximum number of odorants towards the olfactory receptors in the biological medium. At the biological level, the high barrier of odorant uptake might be circumvented by the olfactory system via an increased concentration of OBPs at the air-mucus interface. Future studies should thus include a detailed investigation of the transfer of organic molecules at the gas-mucus interface.

Table 2. Relative binding free energy values (in kJ/mol) of the carvone-pOBP complex obtained with the volume-based metadynamics method using a radius of the restraining sphere of 28 Å. The corresponding free energy landscape is shown in Figure 6. The values have been corrected for the change in translational entropy caused by the restraining potential (see Section 3 of the SI for details).

[a]	$\triangle G$MetaD	$T\triangle S$[b]
(R)-Carvone	−18.16	75.44
(S)-Carvone	−18.03	71.71

[a] Relative energies are given with respect to the unbound state set to 0.00 kJ/mol. [b] Transition state joining the bound and unbound state (see Figure 6).

Conclusion and Outlook

Characterizing the Driving Force of Odorant Transport

Using pOBP and carvone as molecular targets, we set up a multi-scale bottom-up approach to elucidate how OBPs are able to facilitate the transport of odorants through the hydrophilic nasal mucus. Our hypothesis is that due to their strongly hydrophobic beta-barrel binding cavity, OBPs facilitate the transport of hydrophobic odorants though the nasal mucus by lowering the energy barrier at the air-mucus interface. This is achieved by mimicking the gas-phase environment inside the binding pocket, thus allowing the odorant to explore its full conformational flexibility inside the protein. Our multi-scale simulation approach is tailored to monitor the conformational landscape of the odorant carvone throughout the different states it undergoes during the olfactory process: in its isolated state in the gas-phase, in the solvated state, and within the protein environment. Each state requires different computational methods and while the gas phase is best described at quantum chemical level, the solvated phase and the protein environment necessitate computational biology methods such classical molecular dynamics and enhanced sampling techniques. The conformational sampling at quantum chemical level revealed that carvone exhibits six stable energy minima that can be grouped into two distinct structural clusters (named

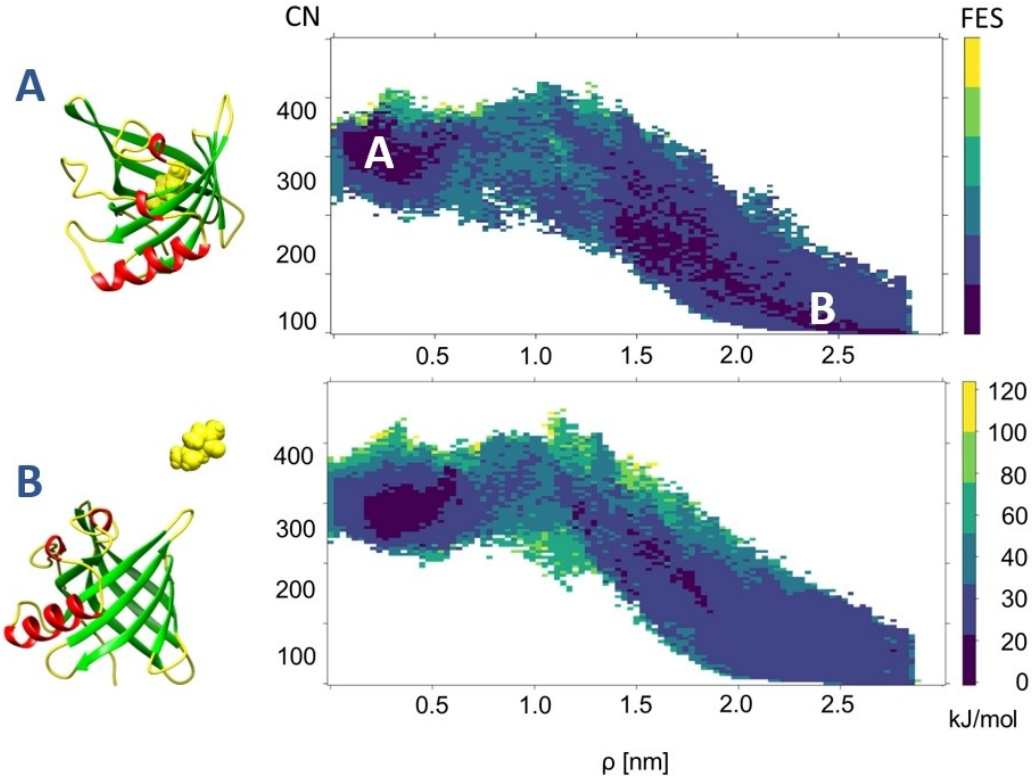

Figure 6. Free energy surface of the pOBP carvone complex generated using volume-based metadynamics for a ρ of 28 Å (Upper trace: *(R)*-carvone. Lower trace: *(S)*-carvone)). CN: coordination number (measure for the number of contacts between the ligand and the protein binding pocket), A and B: bound and unbound states of the pOBP-carvone complex, respectively. See SI for all technical details and the simulation setup.

structural subset I and II, cf. Figure 3). These subsets are distinguishable through the orientation of the isopropenyl moiety of the molecule. To distinguish the different structures within the two subset and monitor changes throughout our simulations, we defined the intramolecular distance *d* as an intrinsic order parameter. To monitor the protein dynamics of the free pOBP, cross barrel distances and the RMSD were used. Our results showed that the structure of pOBP remains unchanged when carvone is bound inside the beta-barrel and no strong interactions could be identified between carvone and protein residues within the binding cavity. As a result, the odorant retains the freedom to sample all the conformations within its conformational space. This complies with the low specificity of OBPs who need to be able to bind a high number of different hydrophobic molecules to fulfill their transporter function. The MD production runs further showed that the conformational space sampled by carvone in the gas-phase during the *in vacuo* simulations strongly resembles the conformations it samples inside the binding cavity of the protein. In both environments, gas-phase and protein, the barrier height for the interconversion is below 10 kJ/mol. In contrast, the barrier height for the interconversion between the different conformers is more than three times higher in explicit water (see Figure 4). This strongly indicates that the hydrophobic environment provided by the protein allows the odorant to maintain its conformational freedom upon binding and directly suggests that the protein environment is more air like. VB metadynamics simulations additionally show that the free energy of the bound state is lower and favors the uptake of the odorant into the hydrophobic cavity. Given that carvone, as most other odorants, is hydrophobic and almost insoluble in water (cf. Table 1), our findings emphasize that OBPs primarily facilitate the uptake of odorants through the mucus layer. Still, this does not exclude the existence of parallel transport mechanisms where odorants may dissolve directly into the hydrophilic mucus and diffuse towards the ORs. However, this alternative route is likely to be kinetically hindered supposing that the purpose of having OBPs in the mucus is to speed up the transport and ultimately the detection of the olfactory signal at receptor level. This view is supported by experiments showing that the olfactory response can also be initiated in the complete absence of OBPs.[39] However, the receptor response is observed at reduced efficiency and sensitivity, which complies with the idea that effectively less odorants will be able cross the air-mucus interface in the absence of OBPs. Finally, being members of the lipocalin super family, it is possible that OBPs take an active part in additional tasks such as a scavenger role during the termination of the olfactory signal,[40] protecting ORs from over saturation, or to participate in the nasal immune response by binding to pathogens or their products.[41]

Future Perspectives: Paving the Way towards Biosensors and Artificial Olfaction

Finally, our study provides new atomistic insight on the transporter function of OBPs which constitute the very first step in the biological process of olfaction. This is a stepping stone that paves the way to fully understand the complex molecular action mechanisms underlying the olfactory sense. In the long run, it is crucial to exploit this challenging biological process for reverse engineering to develop biosensors and to digitize the sense of smell. Due to their compact beta-barrel structure and the resulting exceptional stability towards thermal and chemical denaturation, OBPs seems to be the ideal candidates for application in artificial noses.[42,43] Although the binding of the odorants inside their binding pocket is non-specific,[31] it is possible to fine-tune the physical properties of the binding pocket through point mutations to enhance the binding specificity towards selected molecules. While wild-type pOBP exhibits no binding preferences towards any of the carvone enantiomers, its F88 W mutant was shown to successfully distinguish between the *(R)*- and *(S)*-enantiomer of carvone, and was used as a first bio-electronic capacitance-modulated transistor.[4] A recent study further showed that isoleucines within the pOBP binding pocket are crucial for the chiral discrimination of menthol and carvone.[2] Therefore, OBPs have moved more and more into the center of attention as potential odorant and biomarker detectors.[4,44] However, to exploit these protein targets, further understanding their structure and dynamics is essential to tune their physical properties, i. e., the binding affinity and specificity, towards detecting targeted biomarkers and relevant odorant families. Our work provides new insight into the mechanisms of the odorant uptake through OBPs. In future, it will be necessary to go beyond targeting singled-out OBP-odorant complexes and adapt more global approaches that comprise larger protein and odorant data pools. With the release of AlphaFold structures[45] and sophisticated algorithms such as AlphaFill,[46] larger protein structural databases are becoming available and will allow employ machine learning approaches to rationalize the process of protein design and fine-tune OBPs to selectively target relevant molecular family. In near future, odorant uptake and absorption into the body is likely to gain importance and further open new possibilities and challenges for interdisciplinary research and multi-scale approaches, including, but not limited to the study of the function and mechanisms of the biotransformation of odorants.[47] In any case, quantifying and digitizing the olfactory sense will certainly remain an ambitious goal that requires the joint effort from all disciplines ranging from fragrance chemistry and structure-odor predictions,[48–50] to molecular and structural biology,[51] neuroscience,[52] evolutionary biology,[53] and psychology.[54]

Acknowledgements

The authors would like to acknowledge the SURFsara compute cluster hosted by SURF and the BAZIS research cluster hosted by VU for the computational time and the provided technical support. M.P. would like to thank the Erasmus + trainee-ship program for funds (personal grant M.P.). H.M. would like to thank the *Koninklijke Nederlandse Akademie van Wetenschappen* and the French *Académie des sciences* (Descartes-Huygens Award 2020).

Conflict of Interests

The authors declare no conflict of interest.

Data Availability Statement

The data that support the findings of this study are available in the supplementary material of this article.

Keywords: Odorant Binding · High-Resolution Spectroscopy · Carvone · Enhanced Sampling · Biosensors

[1] P. Pelosi, W. Knoll, *Biol. Rev.* **2022**, *97*, 20.
[2] V. Zaremska, J. Tan, S. Lim, W. Knoll, P. Pelosi, *Chem. Eur. J.* **2020**, *26*, 8720.
[3] J. M. Heydel, A. Coelho, N. Thiebaud, A. Legendre, A. M. L. Bon, P. Faure, F. Neiers, Y. Artur, J. Golebiowski, L. Briand, *Anat. Rec.* **2013**, *296*, 1333.
[4] M. Y. Mulla, E. Tuccori, M. Magliulo, G. Lattanzi, G. Palazzo, K. Persaud, L. Torsi, *Nat. Commun.* **2015**, *6*, 6010.
[5] S. Spinelli, R. Ramoni, S. Grolli, J. Bonicel, C. Cambillau, M. Tegoni, *Biochemistry* **1998**, *37*, 7913.
[6] K. Ahmad, A. Rizzi, R. Capelli, D. Mandelli, W. Lyu, P. Carloni, *Front. Mol. Biosci.* **2022**, *9*, 556.
[7] J. Hénin, T. Lelièvre, M. R. Shirts, O. Valsson, L. Delemotte, *LiveCoMS* **2022**, *4*, 1583.
[8] R. Dahmani, H. Sun, H. Mouhib, *Phys. Chem. Chem. Phys.* **2020**, *22*, 27850.
[9] H. Mouhib, W. Stahl, M. Lüthy, M. Büchel, P. Kraft, *Angew. Chem. Int. Ed.* **2011**, *50*, 5576.
[10] M. Juanes, A. Lesarri, R. Pinacho, E. Charro, J. E. Rubio, L. Enríquez, M. Jaraíz, *Chem. Eur. J.* **2018**, *24*, 6564.
[11] C. Calabrese, P. Écija, I. Compañón, M. Vallejo-López, Álvaro Cimas, M. Parra, F. J. Basterretxea, J. I. Santos, J. Jiménez-Barbero, A. Lesarri, F. Corzana, E. J. Cocinero, *J. Phys. Chem. Lett.* **2019**, *10*, 3339.
[12] N. Mazo, C. D. Navo, F. Peccati, J. Andreo, C. Airoldi, G. Goldsztejn, P. Çarçabal, I. Usabiaga, M. Sodupe, S. Wuttke, J. H. Busto, J. M. Peregrina, E. J. Cocinero, G. Jiménez-Osés, S. G. Jiménez, *Chem. Eur. J.* **2023**, *29*, e202202913.
[13] H. Wang, J. Chen, Y. Zheng, D. A. Obenchain, X. Xu, Q. Gou, J.-U. Grabow, W. Caminati, *J. Phys. Chem. Lett.* **2022**, *13*, 149.
[14] F. Torres-Hernández, P. Pinillos, W. Li, R. Saragi, A. Lesarri, *J. Phys. Chem. Lett.* **2024**, *15*, 5674.
[15] X. Zhang, X. Tian, J. Li, M. Li, T. Gao, S. Zou, J. Chen, X. Xu, Q. Gou, J.-U. Grabow, *J. Phys. Chem. Lett.* **2023**, *14*, 604.
[16] I. Uriarte, A. Insausti, E. J. Cocinero, A. Jabri, I. Kleiner, H. Mouhib, I. Alkorta, *J. Phys. Chem. Lett.* **2018**, *9*, 5906.
[17] S. R. Domingos, C. Pérez, C. Medcraft, P. Pinacho, M. Schnell, *Phys. Chem. Chem. Phys.* **2016**, *18*, 16682.
[18] M. Juanes, I. Usabiaga, I. León, L. Evangelisti, J. A. Fernández, A. Lesarri, *Angew. Chem. Int. Ed.* **2020**, *59*, 14081.
[19] M. Li, W. Li, C. Pérez, A. Lesarri, J.-U. Grabow, *Angew. Chem. Int. Ed.* **2024**, *63*, e202404447.
[20] J. Millan, A. Lesarri, J. A. Fernández, R. Martínez, *ChemBioChem* **2021**, *22*, 408.
[21] J. R. A. Moreno, T. R. Huet, J. J. L. González, *Struct. Chem.* **2013**, *24*, 1163.
[22] F. Partal Ureña, J. R. A. Moreno, J. J. López González, *Tetrahedron: Asymmetry* **2009**, *20*, 89.
[23] R. Capelli, P. Carloni, M. Parrinello, *J. Phys. Chem. Lett.* **2019**, *10*, 3495.

[24] W. Kohn, A. D. Becke, R. G. Parr, *J. Phys. Chem.* **1996**, *100*, 12974–12980.
[25] A. D. Becke, *Phys. Rev. A* **1988**, *38*, 3098–3100.
[26] C. Moller, M. S. Plesset, *Phys. Rev.* **1934**, *46*, 618–622.
[27] M. J. Frisch, G. W. Trucks, H. B. Schlegel, G. E. Scuseria, M. A. Robb, J. R. Cheeseman, G. Scalmani, V. Barone, G. A. Petersson, H. Nakatsuji, X. Li, M. Caricato, A. V. Marenich, J. Bloino, B. G. Janesko, R. Gomperts, B. Mennucci, H. P. Hratchian, J. V. Ortiz, A. F. Izmaylov, J. L. Sonnenberg, D. WilliamsYoung, F. Ding, F. Lipparini, F. Egidi, J. Goings, B. Peng, A. Petrone, T. Henderson, D. Ranasinghe, V. G. Zakrzewski, J. Gao, N. Rega, G. Zheng, W. Liang, M. Hada, M. Ehara, K. Toyota, R. Fukuda, J. Hasegawa, M. Ishida, T. Nakajima, Y. Honda, O. Kitao, H. Nakai, T. Vreven, K. Throssell, J. A. Montgomery, Jr., J. E. Peralta, F. Ogliaro, M. J. Bearpark, J. J. Heyd, E. N. Brothers, K. N. Kudin, V. N. Staroverov, T. A. Keith, R. Kobayashi, J. Normand, K. Raghavachari, A. P. Rendell, J. C. Burant, S. S. Iyengar, J. Tomasi, M. Cossi, J. M. Millam, M. Klene, Adamo, R. Cammi, J. W. Ochterski, R. L. Martin,K. Morokuma, O. Farkas, J. B. Foresman, D. J. Fox, GAUSSIAN **2016**, gaussian Inc. Wallingford CT.
[28] R. Ramoni, S. Spinelli, S. Grolli, V. Conti, E. Merli, C. Cambillau, M. Tegoni, *Biochim. Biophys. Acta Proteins Proteomics* **2008**, *1784*, 651.
[29] M. Perduca, F. Mancia, R. D. Giorgio, H. L. Monaco, *Proteins* **2000**, *42*, 201.
[30] F. Gonçalves, T. G. Castro, N. G. Azoia, A. Ribeiro, C. Silva, A. Cavaco-Paulo, *Sci. Rep.* **2018**, *8*, 1.
[31] F. Vincent, S. Spinelli, R. Ramoni, S. Grolli, P. Pelosi, C. Cambillau, M. Tegoni, *J. Mol. Biol.* **2000**, *300*, 127.
[32] P.-L. Chau, *Mol. Phys.* **1996**, *89*, 1033.
[33] M. Hillyer, B. C. Gibb, *Annu. Rev. Phys. Chem.* **2016**, *67*, 307.
[34] A. K. Felice, C. Schuster, A. Kadek, F. Filandr, C. V. Laurent, S. Scheiblbrandner, L. Schwaiger, F. Schachinger, D. Kracher, C. Sygmund, P. Man, P. Halada, C. Oostenbrink, R. Ludwig, *ACS Catal.* **2021**, *11*, 517.
[35] F. Bianchi, S. Flisi, M. Careri, N. Riboni, S. Resimini, A. Sala, V. Conti, M. Mattarozzi, S. Taddei, C. Spadini, G. Basini, S. Grolli, C. S. Cabassi, R. Ramoni, *PLoS One* **2019**, *14*, e0213545.
[36] R. Capelli, A. Bochicchio, G. Piccini, R. Casasnovas, P. Carloni, M. Parrinello, *J. Chem. Theory Comput.* **2019**, *15*, 3354.
[37] Q. Zhao, R. Capelli, P. Carloni, B. Lüscher, J. Li, G. Rossetti, *J. Chem. Theory Comput.* **2021**, *17*, 7899.
[38] S. Raniolo, V. Limongelli, *Nat. Protoc.* **2020**, *15*, 2837.
[39] S. Xiao, J. S. Sun, J. R. Carlson, *eLife* **2019**, *8*.
[40] S. Grolli, E. Merli, V. Conti, E. Scaltriti, R. Ramoni, *FEBS J.* **2006**, *273*, 5131.
[41] P. Pelosi, W. Knoll, *Biol. Rev.* **2022**, *97*, 20.
[42] M. Staiano, S. D'Auria, A. Varriale, M. Rossi, A. Marabotti, C. Fini, O. V. Stepanenko, I. M. Kuznetsova, K. K. Turoverov, *Biochemistry* **2007**, *46*, 11120.
[43] P. Pelosi, J. Zhu, W. Knoll, P. Pelosi, J. Zhu, W. Knoll, *Sensors* **2018**, *18*, 3248.
[44] A. Nunes-Alves, D. B. Kokh, R. C. Wade, *Curr. Res. Struct. Biol.* **2021**, *3*, 106.
[45] J. Abramson, J. Adler, J. Dunger, R. Evans, T. Green, A. Pritzel, O. Ronneberger, L. Willmore, A. J. Ballard, J. Bambrick, S. W. Bodenstein, D. A. Evans, C.-C. Hung, M. O'Neill, D. Reiman, K. Tunyasuvunakool, Z. Wu, A. Žemgulyte•, E. Arvaniti, C. Beattie, O. Bertolli, A. Bridgland, A. Cherepanov, M. Congreve, A. I. Cowen-Rivers, A. Cowie, M. Figurnov, F. B. Fuchs, H. Gladman, R. Jain, Y. A. Khan, C. M. R. Low, K. Perlin, A. Potapenko, P. Savy, S. Singh, A. Stecula, A. Thillaisundaram, C. Tong, S. Yakneen, E. D. Zhong, M. Zielinski, A. Žídek, V. Bapst, P. Kohli, M. Jaderberg, D. Hassabis, J. M. Jumper, *Nature* **2024**, *630*, 493–500.
[46] M. L. Hekkelman, I. de Vries, R. P. Joosten, A. Perrakis, *Nat. Methods* **2023**, *20*, 205–213.
[47] N. Kornbausch, M. W. Debong, A. Buettner, J.-M. Heydel, H. Loos, *Angew. Chem. Int. Ed.* **2022**.
[48] F. Elterlein, N. Bugdahn, P. Kraft, *Chem. Eur. J.* **2024**, *30*, e202400006.
[49] N. Armanino, J. Charpentier, F. Flachsmann, A. Goeke, M. Liniger, P. Kraft, *Angew. Chem. Int. Ed.* **2020**, *59*, 16310.
[50] B. K. Lee, E. J. Mayhew, B. Sanchez-Lengeling, J. N. Wei, W. W. Qian, K. A. Little, M. Andres, B. B. Nguyen, T. Moloy, J. Yasonik, J. K. Parker, R. C. Gerkin, J. D. Mainland, A. B. Wiltschko, *Science* **2023**, *381*, 999.
[51] L. Guo, J. Cheng, S. Lian, Q. Liu, Y. Lu, Y. Zheng, K. Zhu, M. Zhang, Y. Kong, C. Zhang, N. Rong, Y. Zhuang, G. Fang, J. Jiang, T. Zhang, X. Han, Z. Liu, M. Xia, S. Liu, L. Zhang, S. D. Liberles, X. Yu, Y. Xu, F. Yang, Q. Li, J.-P. Sun, *Nature* **2023**, *618*, 193.
[52] J. D. Zak, G. Reddy, V. Konanur, V. N. Murthy, *Nat. Commun.* **2024**, *15*, 3268.
[53] L. R. Saraiva, F. Riveros-McKay, M. Mezzavilla, E. H. Abou-Moussa, C. J. Arayata, M. Makhlouf, C. Trimmer, X. Ibarra-Soria, M. Khan, L. V. Gerven, M. Jorissen, M. Gibbs, C. O'Flynn, S. McGrane, P. Mombaerts, J. C. Marioni, J. D. Mainland, D. W. Logan, *Sci. Adv.* **2019**, *5*, eaax0396.
[54] Y. Ye, Y. Wang, Y. Zhuang, H. Tan, Z. Zuo, H. Yun, K. Yuan, W. Zhou, *Nat. Hum. Behav.* **2024**, *8*, 1150.

Manuscript received: August 14, 2024
Accepted manuscript online: November 7, 2024
Version of record online: December 4, 2024